REPORT DOCUMENTATION PAGE		Form Approved OMB No. 0704-0188

The public reporting burden for this collection of information is estimated to average 1 hour per response, including the time for reviewing instructions, searching existing data sources, gathering and maintaining the data needed, and completing and reviewing the collection of information. Send comments regarding this burden estimate or any other aspect of this collection of information, including suggestions for reducing the burden, to the Department of Defense, Executive Services and Communications Directorate (0704-0188). Respondents should be aware that notwithstanding any other provision of law, no person shall be subject to any penalty for failing to comply with a collection of information if it does not display a currently valid OMB control number.
PLEASE DO NOT RETURN YOUR FORM TO THE ABOVE ORGANIZATION.

1. REPORT DATE (DD-MM-YYYY) Oct 16, 2012	2. REPORT TYPE Final Report	3. DATES COVERED (From - To) May 2010 - Oct 2012

4. TITLE AND SUBTITLE	5a. CONTRACT NUMBER
Coupling of Peridynamics and Finite Element Formulation for Multiscale Simulations	FA9550-10-1-0222
	5b. GRANT NUMBER
	5c. PROGRAM ELEMENT NUMBER

6. AUTHOR(S)	5d. PROJECT NUMBER
Jung-Wuk Hong	
	5e. TASK NUMBER
	5f. WORK UNIT NUMBER

7. PERFORMING ORGANIZATION NAME(S) AND ADDRESS(ES)	8. PERFORMING ORGANIZATION REPORT NUMBER
Department of Civil & Environmental Engineering Michigan State University East Lansing, MI	

9. SPONSORING/MONITORING AGENCY NAME(S) AND ADDRESS(ES)	10. SPONSOR/MONITOR'S ACRONYM(S)
Air Force Office of Scientific Research 875 N. Randolph Street Arlington, VA 22203 Dr. David Stargel/RSA	
	11. SPONSOR/MONITOR'S REPORT NUMBER(S) AFRL-OSR-VA-TR-2012-1138

12. DISTRIBUTION/AVAILABILITY STATEMENT

Distribution A: Approved for public release, distribution unlimited

13. SUPPLEMENTARY NOTES

14. ABSTRACT

The tasks outlined in the original proposal for two years are: (1) literature review and development of a peridynamic solver, (2) development of an automatic volume calculation routine using the partition of unity principle, (3) numerical testing for different grid widths to horizon ratios, (4) development of an approach to add another material variable in the given approach, (5) preparation of the imaging system for experimental testing, (6) development of peridynamic and finite element coupling module, (7) parallelization of the solvers, (8) verification of the coupled code, and (9) preparation of the imaging system. As for the literature review for the peridynamic formulation, intensive study has been conducted.

15. SUBJECT TERMS

16. SECURITY CLASSIFICATION OF:			17. LIMITATION OF ABSTRACT	18. NUMBER OF PAGES	19a. NAME OF RESPONSIBLE PERSON
a. REPORT	b. ABSTRACT	c. THIS PAGE			
U	U	U	U		19b. TELEPHONE NUMBER (Include area code)

Reset	Standard Form 298 (Rev. 8/98) Prescribed by ANSI Std. Z39.18

INSTRUCTIONS FOR COMPLETING SF 298

1. REPORT DATE. Full publication date, including day, month, if available. Must cite at least the year and be Year 2000 compliant, e.g. 30-06-1998; xx-06-1998; xx-xx-1998.

2. REPORT TYPE. State the type of report, such as final, technical, interim, memorandum, master's thesis, progress, quarterly, research, special, group study, etc.

3. DATES COVERED. Indicate the time during which the work was performed and the report was written, e.g., Jun 1997 - Jun 1998; 1-10 Jun 1996; May - Nov 1998; Nov 1998.

4. TITLE. Enter title and subtitle with volume number and part number, if applicable. On classified documents, enter the title classification in parentheses.

5a. CONTRACT NUMBER. Enter all contract numbers as they appear in the report, e.g. F33615-86-C-5169.

5b. GRANT NUMBER. Enter all grant numbers as they appear in the report, e.g. AFOSR-82-1234.

5c. PROGRAM ELEMENT NUMBER. Enter all program element numbers as they appear in the report, e.g. 61101A.

5d. PROJECT NUMBER. Enter all project numbers as they appear in the report, e.g. 1F665702D1257; ILIR.

5e. TASK NUMBER. Enter all task numbers as they appear in the report, e.g. 05; RF0330201; T4112.

5f. WORK UNIT NUMBER. Enter all work unit numbers as they appear in the report, e.g. 001; AFAPL30480105.

6. AUTHOR(S). Enter name(s) of person(s) responsible for writing the report, performing the research, or credited with the content of the report. The form of entry is the last name, first name, middle initial, and additional qualifiers separated by commas, e.g. Smith, Richard, J, Jr.

7. PERFORMING ORGANIZATION NAME(S) AND ADDRESS(ES). Self-explanatory.

8. PERFORMING ORGANIZATION REPORT NUMBER. Enter all unique alphanumeric report numbers assigned by the performing organization, e.g. BRL-1234; AFWL-TR-85-4017-Vol-21-PT-2.

9. SPONSORING/MONITORING AGENCY NAME(S) AND ADDRESS(ES). Enter the name and address of the organization(s) financially responsible for and monitoring the work.

10. SPONSOR/MONITOR'S ACRONYM(S). Enter, if available, e.g. BRL, ARDEC, NADC.

11. SPONSOR/MONITOR'S REPORT NUMBER(S). Enter report number as assigned by the sponsoring/ monitoring agency, if available, e.g. BRL-TR-829; -215.

12. DISTRIBUTION/AVAILABILITY STATEMENT. Use agency-mandated availability statements to indicate the public availability or distribution limitations of the report. If additional limitations/ restrictions or special markings are indicated, follow agency authorization procedures, e.g. RD/FRD, PROPIN, ITAR, etc. Include copyright information.

13. SUPPLEMENTARY NOTES. Enter information not included elsewhere such as: prepared in cooperation with; translation of; report supersedes; old edition number, etc.

14. ABSTRACT. A brief (approximately 200 words) factual summary of the most significant information.

15. SUBJECT TERMS. Key words or phrases identifying major concepts in the report.

16. SECURITY CLASSIFICATION. Enter security classification in accordance with security classification regulations, e.g. U, C, S, etc. If this form contains classified information, stamp classification level on the top and bottom of this page.

17. LIMITATION OF ABSTRACT. This block must be completed to assign a distribution limitation to the abstract. Enter UU (Unclassified Unlimited) or SAR (Same as Report). An entry in this block is necessary if the abstract is to be limited.

FINAL REPORT

Coupling of Peridynamics and Finite Element Formulation for Multiscale Simulations

---

Year 2 Report

Jung-Wuk Hong
Assistant Professor

Multiscale/Multiphysics Computational Mechanics Lab
Department of Civil & Environmental Engineering
Michigan State University
East Lansing, MI

1 Executive Summary

This final report summarizes the research carried out from May 2010 to October 2012. The tasks outlined in the original proposal for two years are: (1) literature review and development of a peridynamic solver, (2) development of an automatic volume calculation routine using the partition of unity principle, (3) numerical testing for different grid widths to horizon ratios, (4) development of an approach to add another material variable in the given approach, (5) preparation of the imaging system for experimental testing, (6) development of peridynamic and finite element coupling module, (7) parallelization of the solvers, (8) verification of the coupled code, and (9) preparation of the imaging system. As for the literature review for the peridynamic formulation, intensive study has been conducted. A peridynamic solver has been developed in Fortran, and the effect of the different grid sizes and horizons are investigated for brittle materials. The numerical methodology has been extended to accommodate the plasticity behavior of materials. The peridynamic code is implemented using a graphics processing unit (GPU) for highly parallelized computation. A comparison of stresses and strains by finite element analysis (FEA) and peridynamic solutions is performed for a ductile material. A multiscale procedure is proposed to bridge the material models by means of peridynamic bonds and the corresponding macroscale material model used in the finite element analysis. A numerical scheme to couple the peridynamic nodes and finite elements is developed in Matlab and is verified. From the point of view of experimental work, a high speed camera setup was prepared, and impact tests were conducted. The digital image correlation technique (DIC) was selected to analyze the high speed response of the material. During the phases I and II, four research papers have been submitted to international journals. Three papers have been published, and the last one is under review.

2 Introduction

Fracture is one of major concerns in the engineering field for a long time, and people have made substantial efforts in order to understand material failure. Inglis and Griffith made contributions to the early development of fracture analyses, and Irwin extended the Griffith approach by developing the energy release rate [1]. Fracture mechanics provides a more reliable methodology for engineering designs than the traditional strength based approach. However, classical fracture

mechanics has its limitations. For example, a pre-existing crack needs to be defined, and the fracture propagation zone is required to be small compared to geometrical dimensions [2, 3].

In order to simulate crack growth and material damage, various numerical methods have been studied. The cohesive crack model addresses relationships between the crack opening displacement and the cohesive tractions resisting the separation of cracks [4-6]. The cohesive zone models have been incorporated into finite element (FE) models using interface elements and contact surfaces. The partition of unity finite element method (PUFEM) was presented by Melenk and Babuska [7]. Belytschko and collaborators [8, 9] extensively investigated the partition of unity principle for simulations of fracture problems and developed the extended finite element method (XFEM). The XFEM allows the discontinuity not constrained to element boundaries, and it can model the discontinuity without remeshing [10]. Mariani and Perego [11] presented a method for the simulation of quasi-static cohesive crack propagation using the XFEM for quasi-brittle materials. Cox [10] proposed enrichment functions to represent the discontinuity using an analytical investigation of the cohesive crack problem. Considering the minimization of the total energy of the global system, Meschke and Dumstorff [12] proposed a variational form of XFEM for the propagation of cohesive and cohesionless cracks in quasi-brittle solids. Meshfree and particle methods [13] demonstrate capability for numerical simulations of material failures. Molecular dynamics, for example, is capable of investigating nonlinearities in the vicinity of cracks, the bond breaks between atoms, and the formation of extended defects [14-16]. Research on coupling finite element methods and meshless methods [17, 18] has also been conducted.

A great deal of research effort has been made to study many fracture problems. One common benchmark problem characterized by the mixed mode fracture is the test of a double-edge-notched concrete specimen conducted by Nooru-Mohamed *et al.* [19]. The test of Nooru-Mohamed was adopted by De Borst [20] in the discussion of computational modeling of concrete fracture. For the analyses, the finite element smeared-crack approach with the gradient Rankine plasticity model, Cruch-Crack model, and Ottosen's model has been used for numerical studies of Nooru-Mohamed's experiment by Di Prisco *et al.* [21]. A comparative study of three-dimensional constitutive models for the double-edge-notched test was performed by

Pivonka *et al*. [22]. Gasser and Holzapfel [23] employed the cohesive crack model with the PUFEM for the numerical modeling of the test. The XFEM was utilized by Cox [10], Meschke and Dumstorff [12], and Unger *et al*. [24] for the simulations. An adaptive mesh refinement technique applied to a nonlocal version of anisotropic damage model was employed by Patzák and Jirásek [25]. Réthoré *et al*. [26] used a hybrid analytical and XFEM to study the propagation of curved cracks in the double-edge-notched concrete specimen.

As a reformulated theory of continuum mechanics, peridynamics eliminates the spatial derivatives, and it is valid regardless of discontinuities [27,28]. Therefore, peridynamics is useful to solve problems involving spontaneously emerged discontinuities. With the general applicability of peridynamics, many applications of the method have been studied. Silling and Askari [29] wrote the first paper on the numerical simulation using the peridynamic model. In their work, the bond-based peridynamics is employed to study the convergence in a fracture problem and impact of a sphere on a brittle target. Dayal and Bhattacharya [30] studied the kinetics of phase transformations using peridynamics without any additional kinetic relation or the nucleation criterion. By adding pairwise peridynamic moments, Gerstle *et al*.[31] proposed a micropolar peridynamic model. Other applications of peridynamics include modeling of the structural responses under extreme loading [32], structuralstability and failure analyses [33], fracture analyses [34−37], and nucleation analyses of a crack in a solid body [38]. Peridynamics also has been applied to study the effect of fiber directions in composites on the fracture and damage evolution considering anisotropic properties[39-43]. A generalized formulation of bond-based peridynamics was introduced by Silling *et al.* [44], which is called the state-based peridynamics. The convergence of peridynamic states to classical elasticity was studied by Silling and Lehoucq [45], and it is shown that the peridynamic stress tensor converges to the Piola-Kirchhoff stress tensor as the length scale goes to zero. Using the state-based peridynamic method, Warren *et al.* [46] studied the elastic deformation and fracture of a bar. Littlewood [47] presented fragmentation of an expanding tube modeled with state-based peridynamics. Foster *et al.* [48, 49] studied viscoplasticity and the failure criterion for peridynamic states.

Compared with FEM, peridynamics is computationally expensive. Macek and Silling [50]

implemented peridynamics in a commercial finite element analysis code, ABAQUS, using truss elements. The conventional FE mesh is coupled with the peridynamic truss mesh using the embedded element feature available in the finite element analysis code. Lall *et al.* [51] used the peridynamics based finite element model to study shock and vibration reliability of electronics. Kilic and Madenci [52] presented a coupling approach using overlapping regions in which both peridynamic and FE equations are utilized. Agwai *et al.* [53] and Oterkus [54] employed the submodeling approach to couple the FEM with peridynamics. In their approach, the global analysis by means of finite element analysis is performed first, and then peridynamics is used for submodeling. A morphing strategy based on the energy equivalence was proposed by Lubineau *et al.* [55].

In this research, we introduce a coupling approach of discretized peridynamics with finite elements. Different from the approach in [50, 51] implementing peridynamic model in the framework of the conventional FEM and the submodeling approach [53, 54], the peridynamic subregion is directly coupled to the finite element subregion in the present approach. An interface element is introduced to calculate coupling forces instead of using overlapping regions [52] or the morphing strategy [55] to couple peridynamic and FE subregions. Depending on how coupling forces are divided to FE nodes of an interface element, we further discuss two types of coupling schemes.
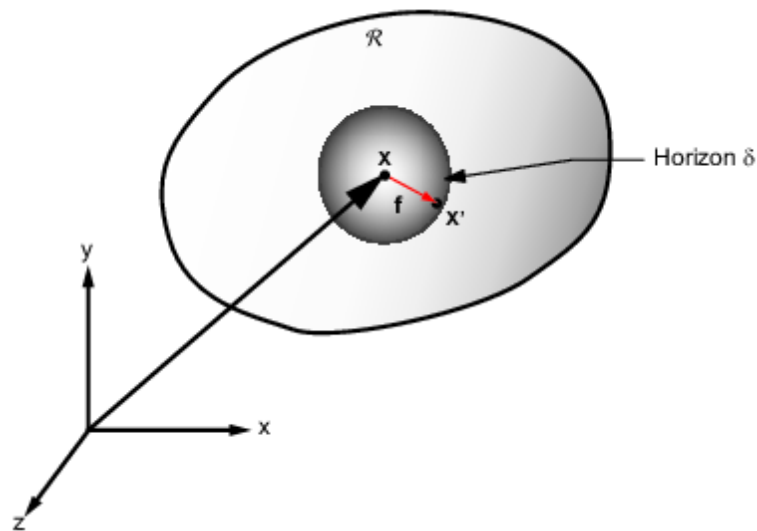

Figure 1: Schematic of peridynamics.

3 Theory

3.1 Peridynamic theory

In the peridynamic theory, the equation of motion of a material point at $\mathbf{x}$ in the reference configuration at time t, as shown in Figure 1, is written as [27, 56, 57]

$$\rho\ddot{\mathbf{u}}(\mathbf{x},t) = \int_{H_{\mathbf{x}}} \mathbf{f}(\boldsymbol{\eta},\boldsymbol{\xi})dV_{\mathbf{x}'} + \mathbf{b}(\mathbf{x},t), \tag{1}$$

where ρ is the mass density, $\mathbf{u}$ is the displacement vector, $\mathbf{f}$ is a pairwise force vector that the material point at $\mathbf{x}'$ exerts on the material point at $\mathbf{x}$, $H_{\mathbf{x}}$ is a neighborhood of the material point at $\mathbf{x}$, and $\mathbf{b}$ is the body force density field. The relative position vector in the reference configuration is expressed as [29]

$$\boldsymbol{\xi} = \mathbf{x}' - \mathbf{x}, \tag{2}$$

and the relative displacement vector at time t is written as

$$\boldsymbol{\eta} = \mathbf{u}(\mathbf{x}',t) - \mathbf{u}(\mathbf{x},t). \tag{3}$$

For each material, a scalar δ, called the horizon, is assumed to exist to determine the interacting spatial range between the material point at $\mathbf{x}$ and the material point at $\mathbf{x}'$ such that

$$\mathbf{f}(\boldsymbol{\eta},\boldsymbol{\xi}) = \mathbf{0} \ \forall \boldsymbol{\eta} \qquad \text{if } \|\boldsymbol{\xi}\| > \delta, \tag{4}$$

where $\|\cdot\|$ is the Euclidean norm. The pairwise force vector $\mathbf{f}$ in the bond-based peridynamics is expressed as

$$\mathbf{f}(\boldsymbol{\eta},\boldsymbol{\xi}) = f(\boldsymbol{\eta},\boldsymbol{\xi})\frac{\boldsymbol{\eta}+\boldsymbol{\xi}}{\|\boldsymbol{\eta}+\boldsymbol{\xi}\|}, \tag{5}$$

where f is a scalar-valued pairwise force. The bond stretch s is defined as

$$s(t,\boldsymbol{\eta},\boldsymbol{\xi}) = \frac{\|\boldsymbol{\eta}+\boldsymbol{\xi}\|-\|\boldsymbol{\xi}\|}{\|\boldsymbol{\xi}\|}, \tag{6}$$

where $\|\boldsymbol{\xi}\|$ is the original bond length in the reference configuration, and $\|\boldsymbol{\eta}+\boldsymbol{\xi}\|$ is the deformed bond length. If the bond stretch $s = 0$, then there is no pairwise force f between material points. Figure 2 shows a microbrittle material model defined for peridynamic bonds. The bond force, which is a scalar function of the bond stretch s, is

$$f(\boldsymbol{\eta},\boldsymbol{\xi}) = cs(t,\boldsymbol{\eta},\boldsymbol{\xi})\mu(t,\boldsymbol{\eta},\boldsymbol{\xi}), \tag{7}$$

where c is the micromodulus, and μ is the scalar function to determine the bond failure. The micromodulus c can be determined by equating the strain energy density in the classical elasticity [29] or by numerical calculations [56]. The numerically determined micromoduli, obtained by considering a finite number of bonds within the horizon, are summarized
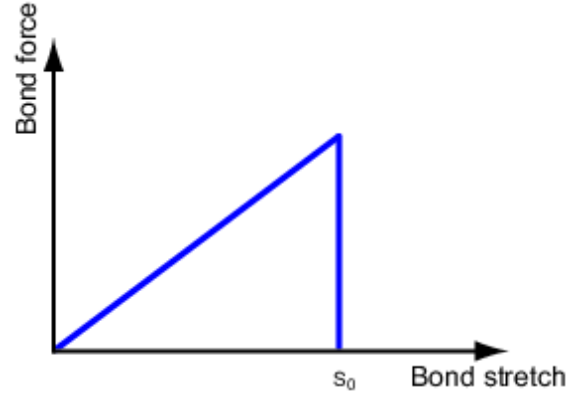

Figure 2: Microbrittle material model.

in Tables 1 and 2 for one- and three-dimensional models, respectively. The critical stretch for bond failure is denoted as s_0. Once a bond fails, it cannot sustain force any more. The critical bond stretch s_0 for microbrittle materials is obtained by setting the work required to break all the bonds per unit fracture area identical to the energy release rate G_f [29]:

$$s_0 = \sqrt{\frac{5G_f}{9k\delta}}. \tag{8}$$

By considering broken bonds, damage dependencies can be introduced into the critical bond stretch [29, 34]. The scalar function μ is related with the critical bond stretch as

$$\mu(t, \boldsymbol{\eta}, \boldsymbol{\xi}) = \begin{cases} 1 & \text{if } s(t', \boldsymbol{\eta}, \boldsymbol{\xi}) < s_0 \quad \text{for all } 0 \le t' \le t, \\ 0 & \text{otherwise.} \end{cases} \tag{9}$$

To solve the peridynamic equation of motion, the material domain is discretized with a number of nodes. The distances of two adjacent nodes are identical over the domain and denoted as Δx. Therefore, the volume representation of each node is $(\Delta x)^3$. The peridynamic equation of motion after discretization is written as

$$\rho \ddot{\mathbf{u}}_I^t = \sum_{J=1}^{N_{\mathrm{H}_I}} \mathbf{f}(\boldsymbol{\eta}^t, \boldsymbol{\xi}) V_J + \mathbf{b}_I^t, \tag{10}$$

where $\ddot{\mathbf{u}}_I^t$ is the acceleration of the node I at time t, $\mathbf{f}(\boldsymbol{\eta}^t, \boldsymbol{\xi})$ is the pairwise force, N_{H_I} is the total number of nodes within the horizon of the node I, and $\mathbf{b}_I^t$ is the body force at time t. The damage index of a node is defined as [29]

$$\varphi(\mathbf{x}_I, t) = 1 - \frac{\sum_{J=1}^{N_{H_I}} \mu(t, \boldsymbol{\eta}, \boldsymbol{\xi}) V_J}{\sum_{J=1}^{N_{H_I}} V_J}. \tag{11}$$

In order to consider the volume reduction of a node that has an intersection with the horizon boundary, a volume reduction scheme [58] is introduced as follows:

Horizon δ	Micromodulus c_1 (N/m^6)
$2\Delta x$	$\dfrac{E}{2\Delta x^4}$
$3\Delta x$	$\dfrac{2E}{9\Delta x^4}$
$4\Delta x$	$\dfrac{E}{8\Delta x^4}$
$5\Delta x$	$\dfrac{2E}{25\Delta x^4}$

Table 1: Micromodulus c_1 in one-dimensional domain.

Horizon δ	Micromodulus c_3 (N/m^6)
$2\Delta x$	$0.302942 \dfrac{E}{\Delta x^4}$
$3\Delta x$	$0.052385 \dfrac{E}{\Delta x^4}$
$4\Delta x$	$0.017290 \dfrac{E}{\Delta x^4}$
$5\Delta x$	$0.006819 \dfrac{E}{\Delta x^4}$

Table 2: Micromodulus c_3 in three-dimensional domain.

$$V_J(\mathsf{P}\xi\mathsf{P}) = \begin{cases} \left(\dfrac{\delta - \mathsf{P}\xi\mathsf{P}}{2r_j} + \dfrac{1}{2}\right)V_J & \text{if } (\delta - r_j)_{,,}\ \mathsf{P}\xi\mathsf{P}_{,,}\ \delta \\[2ex] V_J & \text{if } \mathsf{P}\xi\mathsf{P}_{,,}\ (\delta - r_j), \\[1ex] 0 & \text{otherwise} \end{cases} \tag{12}$$

where $(\delta - r_j)$ is the distance from which the volume is reduced, and r_j is set to be the half of the grid spacing Δx in the numerical implementation.

3.2 Finite element formulations

The equation of motion in the conventional continuum mechanics is derived from the principle of linear momentum. The temporal change rate of linear momentum is equal to the force applied on the body as [59]

$$\rho \ddot{u}_i = \sigma_{ij,j} + f_i^B \qquad \text{in } \Omega, \tag{13}$$

where ρ is the density, $\ddot{u}_i$ is the acceleration field, σ_{ij} is the Cauchy stress tensor, and f_i^B is the body force density field. The essential boundary condition Γ_u and natural boundary condition Γ_f are defined, respectively, as [60]

$$u_i = U_i \qquad \text{on } \Gamma_u, \tag{14}$$

$$\sigma_{ij}n_j = F_i^s \qquad \text{on } \Gamma_f, \tag{15}$$

where the surface of the body $\Gamma = \Gamma_u \cup \Gamma_f$, $\Gamma_u \cap \Gamma_f = 0$, and n_j means the components of the unit outer normal vector on Γ. The constitutive equation for continuum is stated as

$$\sigma_{ij} = C_{ijkl}\varepsilon_{kl}, \tag{16}$$

where C_{ijkl} is the elastic constitutive coefficient, and the components of strains are defined as

$$\varepsilon_{ij} = \frac{1}{2}\left(u_{i,j} + u_{j,i}\right). \tag{17}$$

Applying the principle of virtual work to Equation (13), we have

$$\int_{\Omega}(\sigma_{ij,j} + f_i^B - \rho \ddot{u}_i)\delta u_i d\Omega = 0, \tag{18}$$

where δu_i is the virtual displacement. After integrating by parts and applying the divergence

theorem, the weak formulation is obtained as [61]

$$-\int_{\Omega}\sigma_{ij}\delta u_{i,j}d\Omega+\int_{\Gamma}\sigma_{ij}n_{j}\delta u_{i}dS+\int_{\Omega}f_{i}^{B}\delta u_{i}d\Omega-\int_{\Omega}\rho\ddot{u}_{i}\delta u_{i}d\Omega=0. \tag{19}$$

Considering the symmetry of the stress tensor $(\sigma_{ij}=\sigma_{ji})$ and applying the boundary conditions, we have

$$\int_{\Omega}\rho\ddot{u}_{i}\delta u_{i}d\Omega+\int_{\Omega}\sigma_{ij}\delta\varepsilon_{ij}d\Omega=\int_{\Gamma_{f}}F_{i}^{s}\delta u_{i}dS+\int_{\Omega}f_{i}^{B}\delta u_{i}d\Omega. \tag{20}$$

Substituting the constitutive law in Equation (16) into Equation (20), we obtain the finite element formulation

$$\int_{\Omega}\rho\ddot{u}_{i}\delta u_{i}d\Omega+\int_{\Omega}C_{ijkl}\varepsilon_{kl}\delta\varepsilon_{ij}d\Omega=\int_{\Gamma_{f}}F_{i}^{s}\delta u_{i}dS+\int_{\Omega}f_{i}^{B}\delta u_{i}d\Omega. \tag{21}$$

In the finite element analysis, the displacements within each element are interpolated by means of shape functions as [60]

$$\mathbf{u}^{(e)}=\mathbf{H}^{(e)}\mathbf{U}^{(e)}, \tag{22}$$

where $\mathbf{H}^{(e)}$ is the displacement interpolation matrix, the superscript e represents the element e, and the nodal displacement vector $\mathbf{U}^{(e)}$ is expressed as $\mathbf{U}^{(e)T}=\{u_{1}\ v_{1}\ w_{1}\cdots u_{n}\ v_{n}\ w_{n}\}$ for an element of n nodes. The strain vector is evaluated by

$$\boldsymbol{\varepsilon}^{(e)}=\mathbf{B}^{(e)}\mathbf{U}^{(e)}, \tag{23}$$

where $\mathbf{B}^{(e)}$ is the strain-displacement matrix which is written as

$$\mathbf{B}^{(e)}=\begin{bmatrix}\dfrac{\partial h_{1}}{\partial x} & & & & \dfrac{\partial h_{n}}{\partial x} & \\[2mm] & \dfrac{\partial h_{1}}{\partial y} & & & & \dfrac{\partial h_{n}}{\partial y} \\[2mm] & & \dfrac{\partial h_{1}}{\partial z} & \cdots & & \dfrac{\partial h_{n}}{\partial z} \\[2mm] \dfrac{\partial h_{1}}{\partial y} & \dfrac{\partial h_{1}}{\partial x} & & & \dfrac{\partial h_{n}}{\partial y} & \dfrac{\partial h_{n}}{\partial x} \\[2mm] & \dfrac{\partial h_{1}}{\partial z} & \dfrac{\partial h_{1}}{\partial y} & & \dfrac{\partial h_{n}}{\partial z} & \dfrac{\partial h_{n}}{\partial y} \\[2mm] \dfrac{\partial h_{1}}{\partial z} & & \dfrac{\partial h_{1}}{\partial x} & & \dfrac{\partial h_{n}}{\partial z} & \dfrac{\partial h_{n}}{\partial x} \end{bmatrix}. \tag{24}$$

Substituting Equations (22) and (23) into Equation (21), we have the weak formulation in matrix form as

$$\mathbf{M\ddot{U}} + \mathbf{KU} = \mathbf{F}, \tag{25}$$

where $\mathbf{M}$ is the mass matrix, $\mathbf{K}$ is the stiffness matrix, and $\mathbf{F}$ is the force vector. The assembled matrices following the convention of direct stiffness method [60] are summarized as

$$\mathbf{M} = \sum_e \mathbf{M}^{(e)}, \qquad \mathbf{M}^{(e)} = \int_{\Omega^{(e)}} \rho^{(e)} \mathbf{H}^{(e)T} \mathbf{H}^{(e)} d\Omega^{(e)}, \tag{26}$$

$$\mathbf{K} = \sum_e \mathbf{K}^{(e)}, \qquad \mathbf{K}^{(e)} = \int_{\Omega^{(e)}} \mathbf{B}^{(e)T} \mathbf{C}^{(e)} \mathbf{B}^{(e)} d\Omega^{(e)}, \tag{27}$$

$$\mathbf{F} = \sum_e \mathbf{F}_s^{(e)} + \sum_e \mathbf{F}_B^{(e)},$$
$$\mathbf{F}_s^{(e)} = \int_{\Gamma_f^{(e)}} \mathbf{H}^{(e)T} \mathbf{F}^{S(e)} dS^{(e)}, \qquad \mathbf{F}_B^{(e)} = \int_{\Omega^{(e)}} \mathbf{H}^{(e)T} \mathbf{f}^{B(e)} d\Omega^{(e)}. \tag{28}$$

4 Coupling between the peridynamic and finite element subregions

4.1 Coupling schemes

To gain the efficiency from finite element analyses and exploit the generality of peridynamics in the presence of discontinuities, a domain is partitioned into a conventional FE subregion and a peridynamic subregion as shown in Figure 3. With the coupling approach, the subregion where failure is expected can be modeled using peridynamics. The overall computational cost is reduced by using FEM for the remainder of the domain.
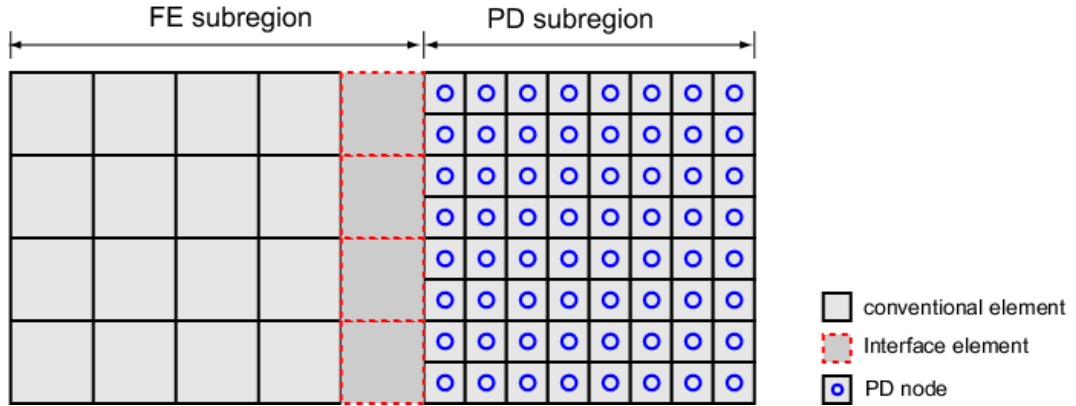

Figure 3: Partitions of the domain. The FE subregion and the peridynamic (PD) subregion are bridged by interface elements.

In the conventional FE subregion, the lumped mass matrix is formed by distributing the total

element mass to nodes of the element [60]. The internal forces on FE nodes can be calculated as

$$\mathbf{F}^{int} = \sum_e \mathbf{F}^{int(e)} = \sum_e \mathbf{K}^{(e)}\mathbf{U}^{(e)}, \qquad (29)$$

where $\mathbf{K}^{(e)}$ is the element stiffness matrix. The equation of motion of an FE node is obtained as

$$M_I\ddot{\mathbf{U}}_I = \mathbf{F}_I^{ext} - \mathbf{F}_I^{int}, \qquad (30)$$

where M_I is the lumped mass of node I, $\ddot{\mathbf{U}}_I$ is the acceleration vector field, $\mathbf{F}_I^{ext}$ is the external force applied on the node I by evaluating the corresponding components of $\mathbf{F}$ in Equation (28), and $\mathbf{F}_I^{int}$ is the internal force vector of the node I. Because the mass matrix is diagonal, Equation (30) can be solved without factorizing a global stiffness matrix.

To bridge the FE subregion and the peridynamic subregion, we introduce an interface element. A three-dimensional interface element consisting of eight FE nodes is illustrated in Figure 5. In an interface element, a number of peridynamic nodes are embedded for the calculation of coupling forces. The interacting forces between embedded peridynamic nodes and peridynamic nodes out of interface elements are called coupling forces. It is worth noting that interactions between embedded peridynamic nodes are not considered as coupling forces. The number of embedded peridynamic nodes is determined by the size of the horizon, and there should be sufficient embedded nodes within the horizon of nodes near the interface of the peridynamic subregion and the FE subregion as shown in Figure 4.
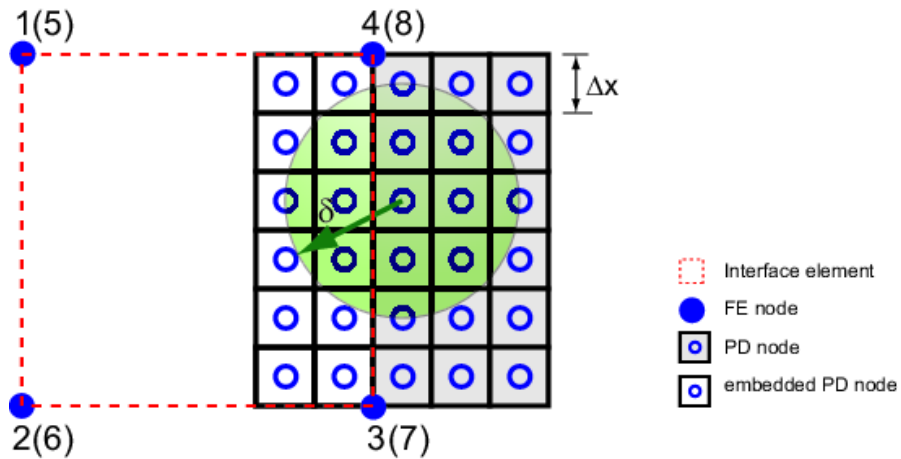

Figure 4: Interface element for the coupling of FE subregion and peridynamic subregion.

To evaluate coupling forces, each embedded peridynamic node represents a material volume of $(\Delta x)^3$ inside an interface element. However, embedded peridynamic nodes are not involved in the global equation. In other words, the displacements of embedded peridynamic nodes are not calculated by solving the equation of motion. Therefore, the mass of an interface element is equally distributed to FE nodes of the interface element. Consider an embedded peridynamic node subjected to the coupling force $\mathbf{f}^{cp}$ as shown in Figure 5, the coupling force is then divided to FE nodes of the interface element by means of shape functions as

$$\mathbf{f}_i^{cp} = \phi_i(\xi, \eta, \psi)\mathbf{f}^{cp}, \qquad i = 1, \cdots, 8, \tag{31}$$

where ϕ_i is the shape function of the node i belonging to the interface element, (ξ, η, ψ) are the natural coordinates of the embedded node in the interface element, which should be determined by the inverse isoparametric mapping. We designate this coupling scheme as the *VL-coupling scheme* since the whole volume of the interface element is subjected to coupling forces. On the other hand, different from the VL-coupling scheme, we might divide coupling forces only to the FE nodes on the interface segment as shown in Figure 6. Therefore, FE nodes not on the interface segment are subjected to internal forces arising from the element stiffness only. Since the interface between the peridynamic and FE subregions is similar to a contact surface, the scheme demonstrated in Figure 6 is designated as the *CT-coupling scheme*. To implement the CT-coupling scheme, interfaces between the peridynamic subregion and the FE subregion have to be defined prior to analyses. Coupling forces on embedded nodes are divided to those FE nodes on the interface segment as shown in Figure 6 by

$$\mathbf{f}_i^{cp} = \phi_i(\xi_c, \eta_c)\mathbf{f}^{cp}, \qquad i = 3, 4, 7, 8, \tag{32}$$

where ϕ_i is the shape function on the interface segment, and (ξ_c, η_c) are the natural coordinates of the projection of an embedded node onto the interface segment.

In general, the equation of motion for FE nodes of an interface element is written as

$$M_I\ddot{\mathbf{U}}_I = \mathbf{F}_I^{ext} - \hat{\mathbf{F}}_I^{int}, \tag{33}$$

where $\mathbf{F}_I^{ext}$ is the external force by evaluating Equation (28), and the internal force is given as

$$\hat{\mathbf{F}}_I^{int} = \mathbf{F}_I^{int} + \mathbf{f}_I^{cp} = \left[\sum_e \mathbf{K}^{(e)}\mathbf{U}^{(e)}\right]_I + \mathbf{f}_I^{cp}, \tag{34}$$

in which $[\cdot]_I$ denotes the corresponding components of a vector associated with the node I of the interface element, and $\mathbf{f}_I^{cp}$ is the summation of coupling forces on the node I. The explicit algorithm is employed for the transient dynamic analyses. Nodal accelerations are calculated first, and nodal velocities and displacements are updated subsequently. After the displacements of FE nodes of the interface elements are calculated, the displacements of embedded peridynamic nodes are then determined by

$$\mathbf{U}_{eb} = \phi_i(\xi,\eta,\psi)\mathbf{U}_i, \qquad i=1,\cdots,8, \tag{35}$$

in which (ξ,η,ψ) are the natural coordinates of an embedded peridynamic node in the interface element, and $\mathbf{U}_i$ is the nodal displacement of an interface element. For peridynamic nodes out of the interface elements, Equation (10) is used to update nodal accelerations.

4.2 *Inverse isoparametric mapping*

To couple peridynamic subregions with finite element subregions, a certain number of peridynamic nodes are embedded in the interface elements. If the Cartesian coordinates of an embedded peridynamic node are known, the natural coordinates of the embedded peridynamic node in an interface element should be determined by the inverse isoparametric mapping, which is essential especially for random discretizations.
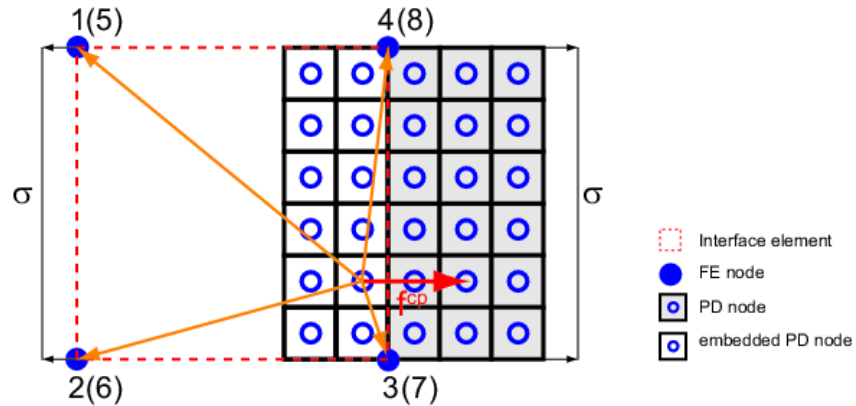

Figure 5: VL-coupling scheme that divides a coupling force $\mathbf{f}^{cp}$ to FE nodes of the interface element.

However, the inverse isoparametric mapping from the Cartesian coordinates to the natural coordinates is nontrivial since equations to be solved are nonlinear. Murti and Valliappan [62] presented a numerical technique by bisecting a line passing a point and a node of known natural coordinates, and this method was extended to the three-dimensional space by Murti *et al.* [63]. However, the bisection method has its limitations [64].
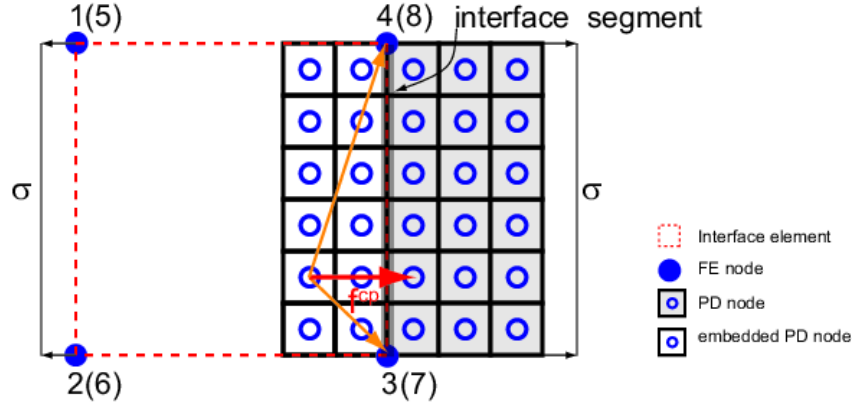

Figure 6: CT-coupling scheme that divides a coupling force $\mathbf{f}^{cp}$ to FE nodes on the interface segment.

A more generalized approach for the inverse isoparametric mapping is presented by Chinnaswamy *et al.* [64]. For the inverse mapping of an embedded peridynamic node with known Cartesian coordinates $(\hat{x}, \hat{y}, \hat{z})$, the equation to be solved is written as

$$
\mathbf{f} = \left\{ \begin{array}{c} f_1(\xi,\eta,\psi) \\ f_2(\xi,\eta,\psi) \\ f_3(\xi,\eta,\psi) \end{array} \right\} = \left\{ \begin{array}{c} \displaystyle\sum_{i=1}^{n} \phi_i(\xi,\eta,\psi)x_i - \hat{x} \\ \displaystyle\sum_{i=1}^{n} \phi_i(\xi,\eta,\psi)y_i - \hat{y} \\ \displaystyle\sum_{i=1}^{n} \phi_i(\xi,\eta,\psi)z_i - \hat{z} \end{array} \right\} = \left\{ \begin{array}{c} 0 \\ 0 \\ 0 \end{array} \right\}, \tag{36}
$$

where (ξ,η,ψ) are the natural coordinates of an embedded peridynamic node in an interface element to be determined. By expanding the vector $\mathbf{f}$ in Taylor's series and omitting the second and higher order terms, it can be shown that [64]

$$\mathbf{I} = \mathbf{I}_0 - \begin{bmatrix} \dfrac{\partial f_1}{\partial \xi} & \dfrac{\partial f_1}{\partial \eta} & \dfrac{\partial f_1}{\partial \psi} \\[2mm] \dfrac{\partial f_2}{\partial \xi} & \dfrac{\partial f_2}{\partial \eta} & \dfrac{\partial f_2}{\partial \psi} \\[2mm] \dfrac{\partial f_3}{\partial \xi} & \dfrac{\partial f_3}{\partial \eta} & \dfrac{\partial f_3}{\partial \psi} \end{bmatrix}_0^{-1} \mathbf{f}_0, \tag{37}$$

where $\mathbf{I}_0 = [\xi_0, \eta_0, \psi_0]^T$ is an approximate solution, and $\mathbf{f}_0$ is the vector $\mathbf{f}$ evaluated at the approximate solution $\mathbf{I}_0$. Equation (37) can be rewritten as

$$\mathbf{I} = \mathbf{I}_0 - \begin{bmatrix} \sum \dfrac{\partial \phi_i}{\partial \xi} x_i & \sum \dfrac{\partial \phi_i}{\partial \eta} x_i & \sum \dfrac{\partial \phi_i}{\partial \psi} x_i \\[2mm] \sum \dfrac{\partial \phi_i}{\partial \xi} y_i & \sum \dfrac{\partial \phi_i}{\partial \eta} y_i & \sum \dfrac{\partial \phi_i}{\partial \psi} y_i \\[2mm] \sum \dfrac{\partial \phi_i}{\partial \xi} z_i & \sum \dfrac{\partial \phi_i}{\partial \eta} z_i & \sum \dfrac{\partial \phi_i}{\partial \psi} z_i \end{bmatrix}_0^{-1} \begin{Bmatrix} \sum \phi_i x_i - \hat{x} \\[1mm] \sum \phi_i y_i - \hat{y} \\[1mm] \sum \phi_i z_i - \hat{z} \end{Bmatrix}_0, \tag{38}$$

and it can be simplified as

$$\mathbf{I} = \mathbf{I}_0 + \Delta\mathbf{I}, \tag{39}$$

where

$$\Delta\mathbf{I} = \begin{Bmatrix} \Delta\xi \\ \Delta\eta \\ \Delta\psi \end{Bmatrix} = -\mathbf{J}_0^{-1}\mathbf{f}_0. \tag{40}$$

The updated solution of $\mathbf{I}$ is used as the value of $\mathbf{I}_0$ in Equation (39) for the next iteration. A few iterations are performed till the solution of $\mathbf{I}$ converges.

If the CT-coupling scheme is employed, coupling forces on embedded peridynamic nodes are only distributed to FE nodes on the interface segment as shown in Figure 6. Hence, the natural coordinates of the projection of an embedded peridynamic node onto the interface segment have to be determined.
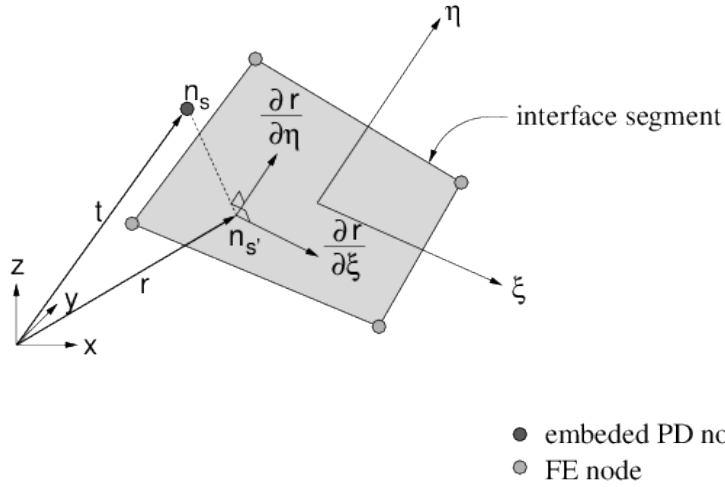
Figure 7: Projection of an embedded peridynamic node on an interface segment.

Let $\mathbf{t}$ be the position vector of an embedded node n_s, and the projection of n_s onto the interface segment is denoted by $n_{s'}$ as shown in Figure 7. The position vector $\mathbf{r}$ of the point $n_{s'}$ on the interface segment can be expressed as

$$\mathbf{r} = f_1(\xi_c, \eta_c)\mathbf{e}_1 + f_2(\xi_c, \eta_c)\mathbf{e}_2 + f_3(\xi_c, \eta_c)\mathbf{e}_3, \tag{41}$$

where (ξ_c, η_c) are the natural coordinates of the point $n_{s'}$ on the interface segment, and

$$f_i(\xi, \eta) = \sum_{j=1}^{4} \phi_j x_i^j, \tag{42}$$

in which ϕ_j is the shape function of the node j on the interface segment. The natural coordinates (ξ_c, η_c) of the point $n_{s'}$ on the interface segment must satisfy [65]

$$\frac{\partial \mathbf{r}}{\partial \xi} \cdot (\mathbf{t} - \mathbf{r}) = 0, \tag{43}$$

$$\frac{\partial \mathbf{r}}{\partial \eta} \cdot (\mathbf{t} - \mathbf{r}) = 0. \tag{44}$$

However, there is no analytical solution to Equations (43) and (44). To solve numerically, a few iterations of the least-squares projection are used to generate an initial guess as

$$\xi_0 = 0, \qquad \eta_0 = 0, \tag{45}$$

$$\begin{bmatrix} \mathbf{r}_{,\xi} \cdot \mathbf{r}_{,\xi} & \mathbf{r}_{,\xi} \cdot \mathbf{r}_{,\eta} \\ \mathbf{r}_{,\eta} \cdot \mathbf{r}_{,\xi} & \mathbf{r}_{,\eta} \cdot \mathbf{r}_{,\eta} \end{bmatrix} \Delta\xi\Delta\eta = -\mathbf{r}_{,\xi} \cdot (\mathbf{r}-\mathbf{t})\mathbf{r}_{,\eta} \cdot (\mathbf{r}-\mathbf{t}), \tag{46}$$

$$\xi_{i+1} = \xi_i + \Delta\xi, \qquad \eta_{i+1} = \eta_i + \Delta\eta. \tag{47}$$

With an initial guess, Newton-Raphson method is then utilized to find the solution of Equations (43) and (44) as [66]

$$\mathbf{H}\Delta\xi\Delta\eta = -\mathbf{r}_{,\xi} \cdot (\mathbf{r}-\mathbf{t})\mathbf{r}_{,\eta} \cdot (\mathbf{r}-\mathbf{t}), \tag{48}$$

$$\mathbf{H} = \begin{bmatrix} \mathbf{r}_{,\xi} \cdot \mathbf{r}_{,\xi} & \mathbf{r}_{,\xi} \cdot \mathbf{r}_{,\eta} \\ \mathbf{r}_{,\eta} \cdot \mathbf{r}_{,\xi} & \mathbf{r}_{,\eta} \cdot \mathbf{r}_{,\eta} \end{bmatrix} + \begin{bmatrix} (\mathbf{r}-\mathbf{t}) \cdot \mathbf{r}_{,\xi\xi} & (\mathbf{r}-\mathbf{t}) \cdot \mathbf{r}_{,\xi\eta} \\ (\mathbf{r}-\mathbf{t}) \cdot \mathbf{r}_{,\xi\eta} & (\mathbf{r}-\mathbf{t}) \cdot \mathbf{r}_{,\eta\eta} \end{bmatrix}, \tag{49}$$

$$\xi_{i+1} = \xi_i + \Delta\xi, \qquad \eta_{i+1} = \eta_i + \Delta\eta. \tag{50}$$

The solutions of ξ_{i+1} and η_{i+1} are used to update the value of the position vector $\mathbf{r}$, and then Equation (48) is evaluated again for the next iteration. The converged solutions of ξ_{i+1} and η_{i+1} are the natural coordinates of the point $n_{s'}$ on the interface segment.

5 Numerical applications

5.1 One-dimensional bar

For benchmarking, the present coupling approach of peridynamics with FEM is employed to study the axial deformation of a one-dimensional bar. The length of the bar is 9.5 mm, and dimensions of the cross section are 0.5 mm by 0.5 mm. Young's modulus E of the bar is 70 GPa, and the density is 2700 kg/m^3. Figure 8 shows the multiscale discretization of the bar. The finite element mesh size is 1.5 mm, and the conventional bar elements are utilized. The stiffness of a bar is $k = \dfrac{EA}{L}$, where A is the cross-sectional area and L is the length of the bar. The peridynamic grid spacing is 0.5 mm, which is equal to the width of the bar. By setting the horizon to $2\Delta x$, the one-dimensional micromodulus c_1 is 5.6×10^{23} N/m^6. Two interface elements are used to couple peridynamic and FE subregions, and each interface element

has two embedded peridynamic nodes for the calculation of coupling forces as shown in Figure 8.
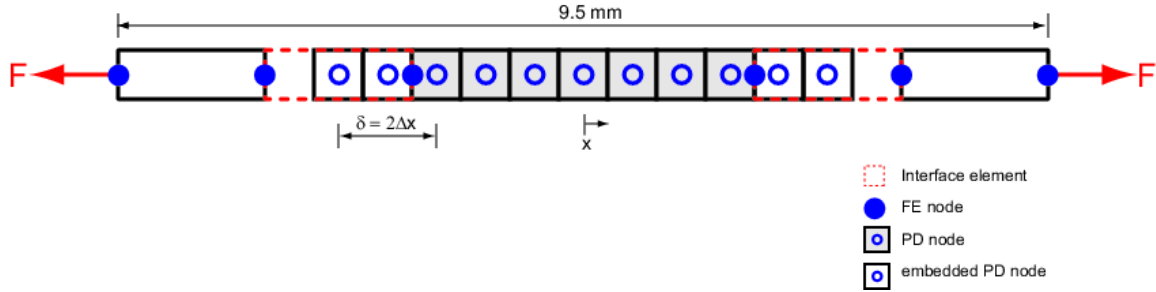

Figure 8: Discretization of a one-dimensional bar for coupling.
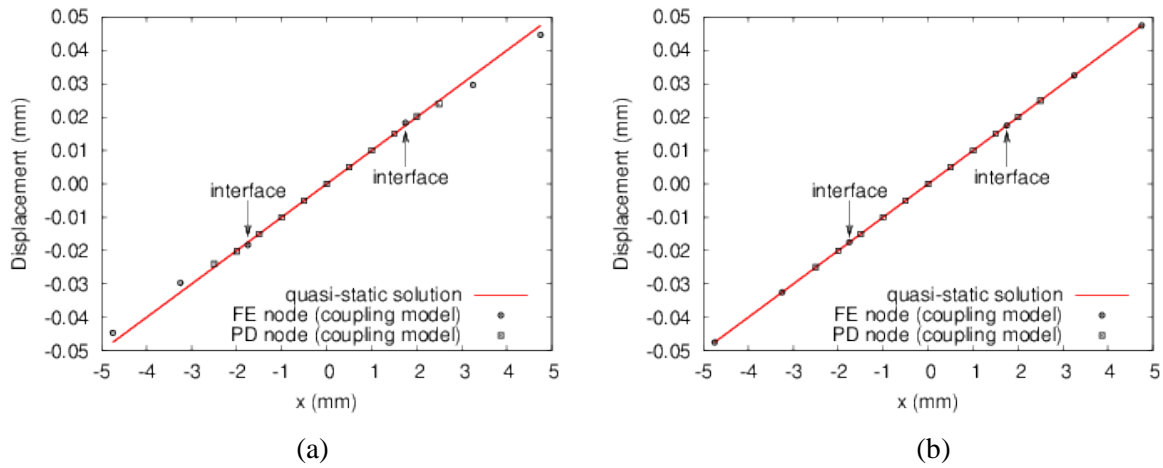

| (a) | (b) |

Figure 9: Axial displacement along the bar using the (a) VL-coupling scheme and (b) CT-coupling scheme.

A tensile loading with the magnitude of $F = 175$ N is applied on both ends of the bar under the quasi-static condition. The force is gradually increased during $50,000$ steps with the calculation time step $dt = 5 \times 10^{-8}$ s, which is less than the critical time step for the explicit time integration. Figure 9(a) shows the displacement along the bar using the VL-coupling scheme. Nodal displacements in the peridynamic subregion show good agreement with the quasi-static solution. The displacements of the FE nodes, however, show small discrepancies. The reason is that coupling forces in an interface element are divided to all FE nodes of the element using the VL-coupling scheme so that FE nodes at the interfaces of subregions ($x = \pm 1.75$ mm) only receive partial coupling forces. FE nodes at the other end of the interface elements ($x = \pm 3.25$

mm) receive the rest of coupling forces, and are also subjected to internal forces arising from the element stiffness. Consequently, the displacements of FE nodes at the interfaces are slightly overestimated, and displacements of other FE nodes are underestimated as indicated in Figure 9(a). In contrast, the solution using the CT-coupling scheme, which distributes coupling forces only to FE nodes at interfaces, is almost identical to the quasi-static solution as shown in Figure 9(b). Hence, for the calculation of axial displacement, the CT-coupling scheme is more effective than the VL-coupling scheme to achieve the coupling between the peridynamic subregion and the FE subregion.
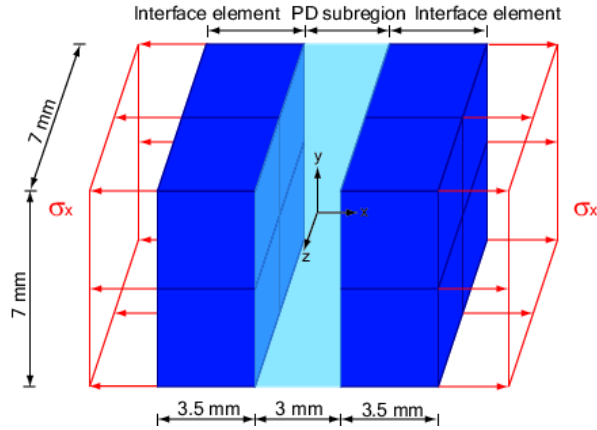
5.2 Three-dimensional bar

Figure 10: Three-dimensional bar subjected to tension.

A three-dimensional bar subjected to tension is examined to compare the solutions of the present coupling approach and the classical (local) elasticity solutions. The dimensions of the bar are taken to be 10 mm in length, 7 mm in width, and 7 mm in thickness as shown in Figure 10. The three-dimensional model is partitioned into two FE subregions and one peridynamic subregion. Each FE subregion consists of four eight-node solid interface elements, and the mesh size of the interface element is 3.5 mm. The peridynamic subregion is uniformly discretized with the grid spacing $\Delta x = 0.5$ mm, and the size of the horizon is set to $\delta = 1.0$ mm. In the interface element, two additional layers of peridynamic nodes are embedded along the longitudinal direction to ensure sufficient nodes in the horizon of peridynamic nodes near the interfaces. Tractions at both end surfaces are gradually applied up to $\sigma_x = 700$ MPa during $100,000$ steps as quasi-static loading, and the calculation time step is set to $dt = 5 \times 10^{-8}$ s. Young's modulus of the bar is 70 GPa, Poisson's ratio is 0.25, and the density is 2700 kg/m3.

We first examine the numerical solutions using the VL-coupling scheme. The longitudinal displacements u_x at three measuring positions are compared to the quasi-static results as shown

in Figure 11(a). The displacement u_x at the position p_1, which is the at the end surface, is underestimated compared to the quasi-static solution. On the other hand, the displacement at p_2, which is at the interface of the peridynamic subregion and the FE subregion, and the displacement at p_3, which is inside the peridynamic subregion, show good agreement with the quasi-static solutions. To look into Poisson effect, the transverse displacements measured at different positions are plotted in Figure 11(b). The transverse displacement q_1 at the end surface is smaller than the quasi-static value since the longitudinal displacement at the end surface is underestimated. Nevertheless, the transverse displacement q_2 at the interface demonstrates close agreement with the quasi-static solution, which indicates that Poisson effect is preserved at the interface. The transverse displacement at q_3, which is inside the peridynamic subregion, also matches the quasi-static solution.

For the comparison of two types of coupling schemes, the CT-coupling scheme, which achieves coupling by considering the interfaces of subregions similar to contact surfaces, is then employed to study this quasi-static problem. As shown in Figure 12(a), the longitudinal displacement p_1 at the end surface is close to the quasi-static solution with the error less than 2%. The longitudinal displacements at interface and inside the peridynamic subregion, denoted by p_2 and p_3 respectively in Figure 12(a), are almost identical to the quasi-static solutions. The transverse displacements measured at different positions are plotted in Figure 12(b). With the improved result in the longitudinal displacement at the end surface, the transverse displacement q_1 at the end surface turns to be very close to the quasi-static solution. On the other hand, the transverse displacement q_2 at the interface is overestimated. This phenomenon occurs due to the reason that decompositions of coupling forces in the transverse direction are divided only to FE nodes on the interface. By comparing Figures 11 and 12, it is observed that the CT-coupling scheme is effective in resolving displacements normal to the interface of peridynamic and FE subregions. On the other hand, the VL-coupling scheme, which divides coupling forces to all FE nodes of the interface element, is capable to preserve Poisson effect at the interface.
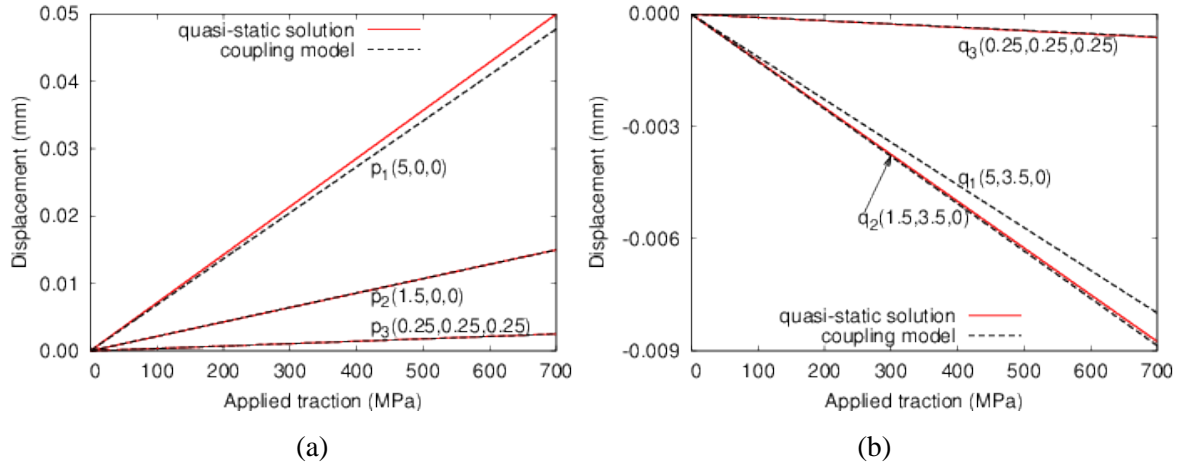
Figure 11: Displacements (a) u_x and (b) u_y at different positions using the VL-coupling scheme. Coordinates of the measuring position are given in parenthesis.
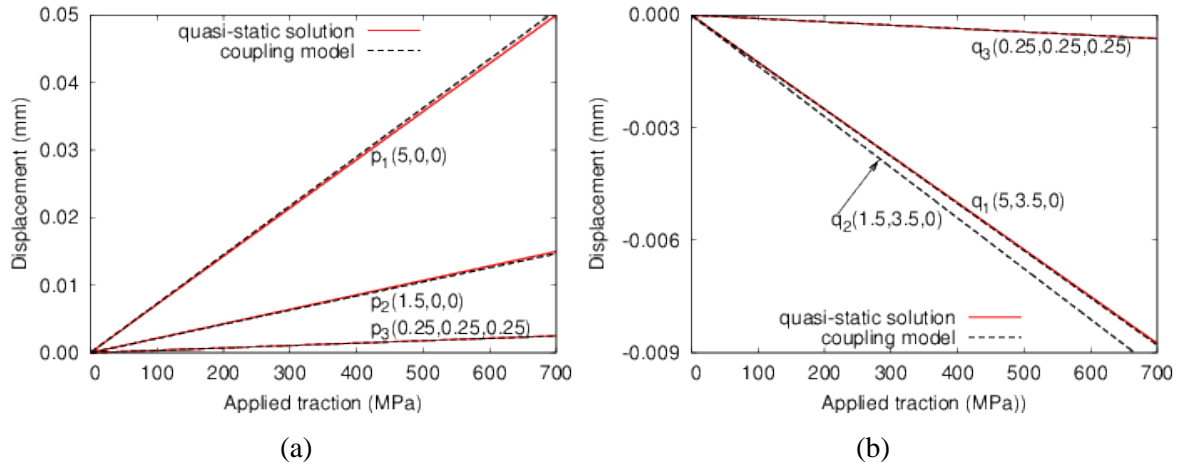

Figure 12: Displacements (a) u_x and (b) u_y at different positions using the CT-coupling scheme. Coordinates of the measuring position are given in parenthesis.
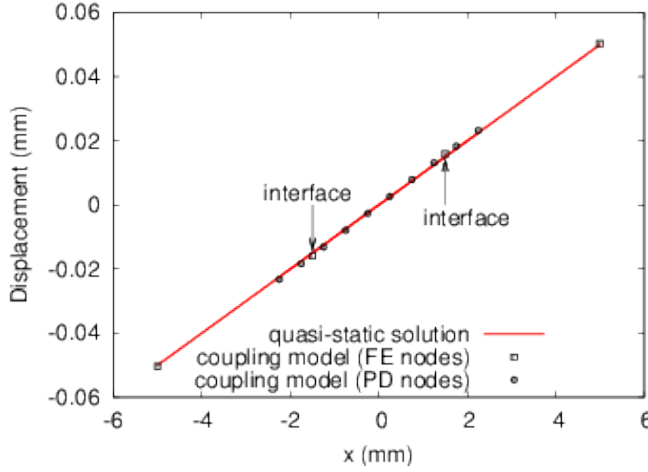
Figure 13: Axial displacement along the edge of the bar using the CT-coupling scheme.

Figure 13 shows the longitudinal displacement along the edge of the bar solved by the CT-coupling scheme. It is noted that a smooth curve can be obtained if the nodal displacements are connected, which is different from the result in [52] where a jump in displacement is observed at the interface. The strain ε_x distributions in the bar and at the interface are plotted in Figure 14. Nodal strains in the FE subregions are obtained by evaluating Equation (23), and nodal strains in the peridynamic subregion are calculated as the average bond stretch within the grid width Δx. Considering the quasi-static condition, the analytical value of strain ε_x is 0.01. The strain of the coupling model is in the range of 0.0099 to 0.0105 as shown in Figure 14, which agrees with the quasi-static solution.
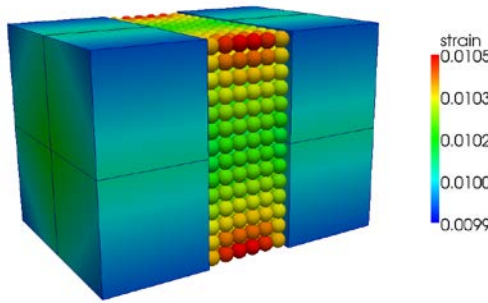
(a)   (b)
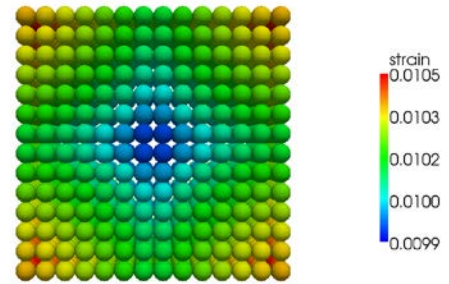
Figure 14: Strain ε_x distributions (a) in the bar and (b) at the interface when the applied traction $\sigma_x = 700$ MPa. The CT-coupling scheme is used in the simulation.
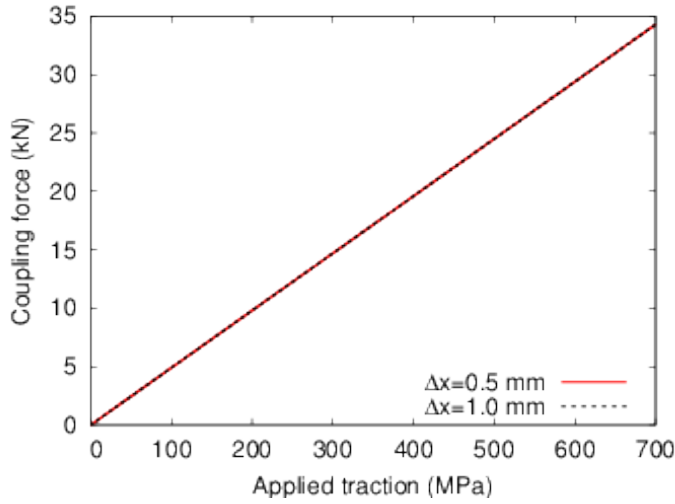
Figure 15: Summation of coupling forces in the longitudinal direction on the interface elements at the left end of the bar. The CT-coupling scheme is used in the simulation.

The essence of coupling forces is interactions between nodes in the peridynamic subregion and material volumes of an adjacent continuous body (i.e. interface elements) represented by embedded peridynamic nodes. Therefore, the ratio of the grid spacing of peridynamic nodes to the mesh size of interface elements should not affect the results. To illustrate this point, Figure 15 shows the summation of coupling forces in the longitudinal direction on the interface elements at the left end of the bar as the applied traction increases. As indicated by the comparison in Figure 15, differences in the results using the grid spacing $\Delta x = 1.0$ mm and $\Delta x = 0.5$ mm are insignificant.

5.3 Mixed mode fracture in a tension-shear specimen

A benchmark problem of mixed mode crack propagation in a concrete specimen has been investigated experimentally by Nooru-Mohamed *et al.* [19]. The double-edge-notched specimen is illustrated in Figure 16(a). The dimensions of the specimen are taken to be 200 mm in both length and height, 50 mm in width, and two notches at edges are 25 mm in length, 5 mm in height, and 50 mm in width. For the numerical study, the specimen is partitioned into two FE subregions and one peridynamic subregion as shown in Figure 16(b). The FE subregion is discretized with two mesh sizes, 10 mm× 10 mm× 16.25 mm and 10 mm× 10 mm× 13 mm. The peridynamic subregion is discretized with the grid spacing $\Delta x = 5.0$ mm, which is $1/10$ of the specimen thickness, and the horizon is set to $\delta = 1.0$ mm. The notches in the peridynamic subregion are introduced by deleting nodes along two notches and removing all bonds across the notches. Since the ratio of the horizon to the grid spacing is equal to two, two

layers of peridynamic nodes adjacent to interfaces are embedded in interface elements for the calculation of coupling forces.
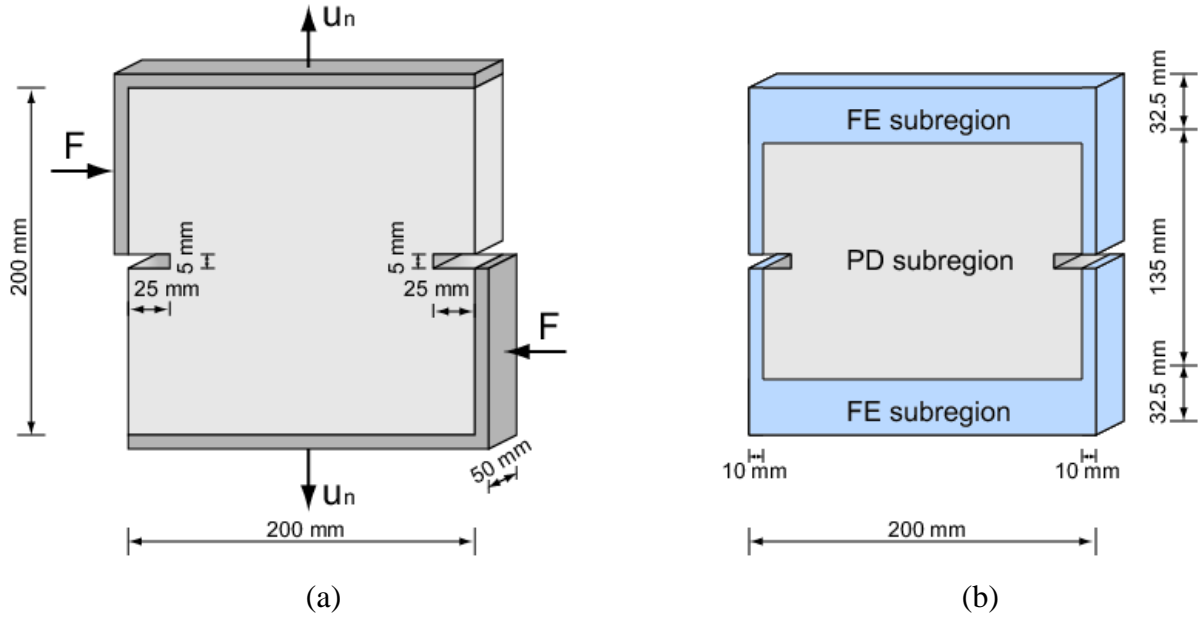

Figure 16: Mixed mode fracture test: (a) geometry of the specimen; (b) subregions of the coupling model.

Young's modulus, Poisson's ratio, and fracture energy were not measured in the experiments. Therefore, we adopt the material properties $E = 30$ GPa and $G_f = 110$ J/m^2 as in [10]. For Poisson's ratio, it is estimated as $v = 0.2$ in the numerical studies in [10, 12], and $v = 0.3$ is used in [67]. In the present study, Poisson's ratio $v = 0.25$ is assumed. The density is calculated from the concrete composition given in [19] as $\rho = 2265$ kg/m^3. By applying Equation (8), the critical bond stretch is obtained as $s_0 = 5.5277 \times 10^{-4}$. The brittle material model illustrated in Figure 2 is utilized for the peridynamic subregion, and the linear elastic model is employed for the remaining FE subregions, where material parameters $E = 30$ GPa and $v = 0.25$ are used.

For the comparison, the load-path 1b (specimen 46-05) in [19] is considered. A horizontal shear force of 10 kN is applied first, and then the vertical displacement u_n is applied on the top and bottom of the specimen as shown in Figure 16(a). In the numerical calculation, the time step is set to $dt = 1 \times 10^{-7}$ s, which is less than the critical time step for the explicit time integration. The vertical displacement u_n is applied by imposing a constant velocity of 10 mm/s as

quasi-static loading. We first examine the numerical predictions of crack paths using the VL-coupling scheme. The cracks initiate near the notches as shown in Figure 17(a), and propagate along the horizontal direction for about 50 mm. As the boundary displacement increases, the direction of propagation changes as shown in Figures 17(b) and 17(c). At the boundary displacement $u_n = 0.09$ mm, two cracks are connected as shown in Figure 17(d). The numerical prediction of crack paths using the VL-coupling scheme shows differences with the experimental observations in [19].

We then apply the CT-coupling scheme for the numerical simulation. Interfaces are predefined in the reference configuration, and there are 280 interface segments with the given mesh sizes. Natural coordinates of the projections of embedded nodes onto interface segments are saved to a list. In the subsequent calculations, the natural coordinates of projected points are referred, and the coupling forces on embedded peridynamic nodes are divided to FE nodes on interface segments. The damage evolution is shown in Figure 18. Crack initiation occurs at the left and right notches as shown in Figure 18(a), and materials ahead of crack tips are damaged for the length of around 15 mm to 20 mm. Due to the angle change of the principal stress, cracks propagate with an angle as shown in Figure 18(b). As the boundary displacement increases, two curvilinear crack paths are clearly observed in Figure 18(c). An enclose area is gradually formed between two curvilinear cracks as indicated in Figure 18(d). The numerical prediction of crack paths shows agreement, especially for the lower crack, with the experimental observation presented in [19], which is illustrated using the solid line in Figure 18(d). The small discrepancies appeared in Figure 18(d) might be caused by the perfectly brittle material model adopted in the numerical simulation. More investigation of material models for concrete in the framework of peridynamics is required in the future. Note that the numerically predicted crack paths are in perfect symmetry. On the contrary, the cracks in the experiment do not show perfect symmetry, and we might speculate on symmetry breaking caused by the slight differences in the loading condition and the material heterogeneity.

Compared to the numerical results using the VL-coupling scheme, the results using the CT-coupling scheme demonstrate better agreement with the experimental observation. The

reason for the inferiority of the VL-coupling scheme in this mixed mode fracture problem is that the horizontal displacement at edges caused by the constant shear loading is underestimated after the applied vertical displacement at boundaries reaches the critical value for the crack initiation at two notches. Consequently, the opening-mode fracture dominates, and the large area ahead of crack tips is damaged in the plane of notches. After the intact region in the middle of the specimen becomes relatively small, rotations of crack paths then take place as shown in Figure 17.

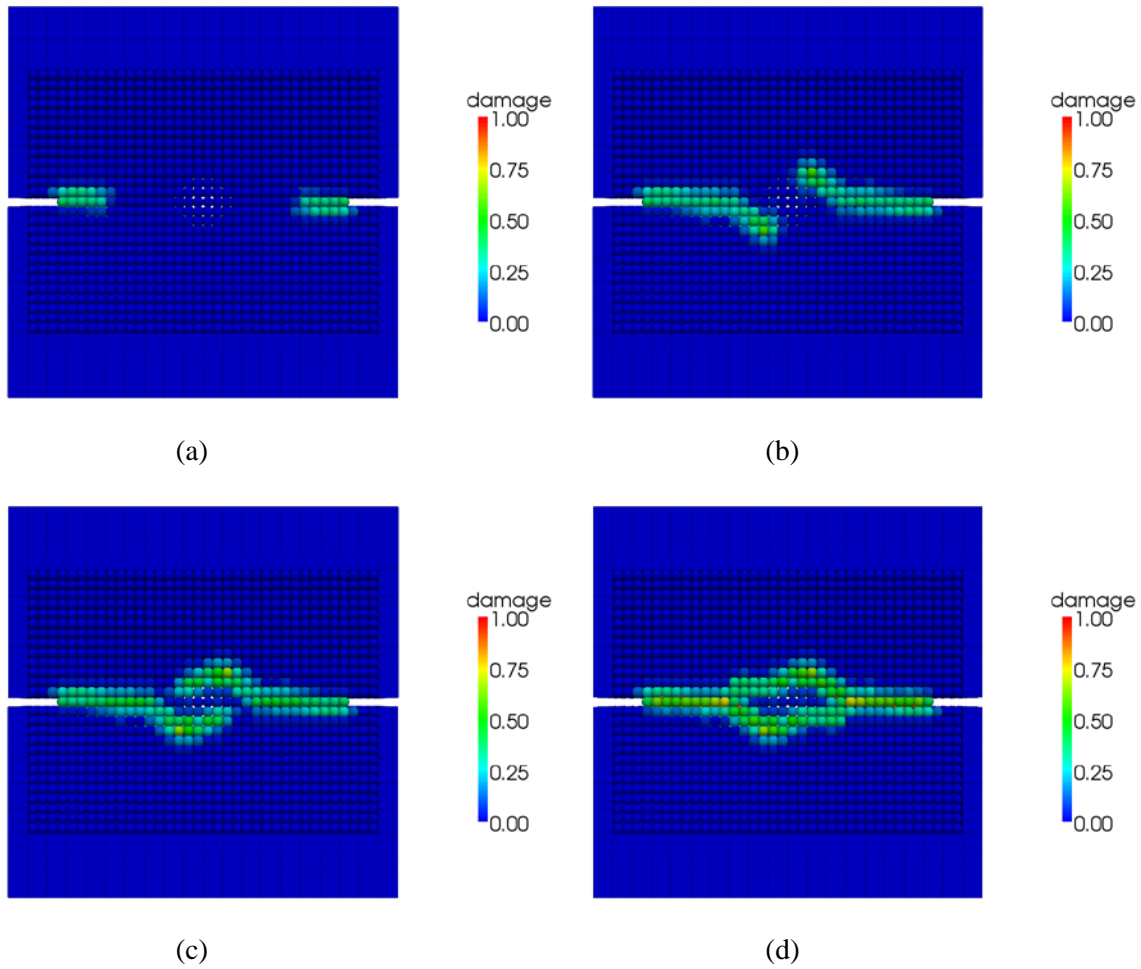| (a)	(b)

(c)	(d)

Figure 17: Numerical prediction of crack paths using the VL-coupling scheme. Boundary displacement: (a) $u_n = 0.0220$ mm; (b) $u_n = 0.0225$ mm; (c) $u_n = 0.03$ mm; (d) $u_n = 0.09$ mm.
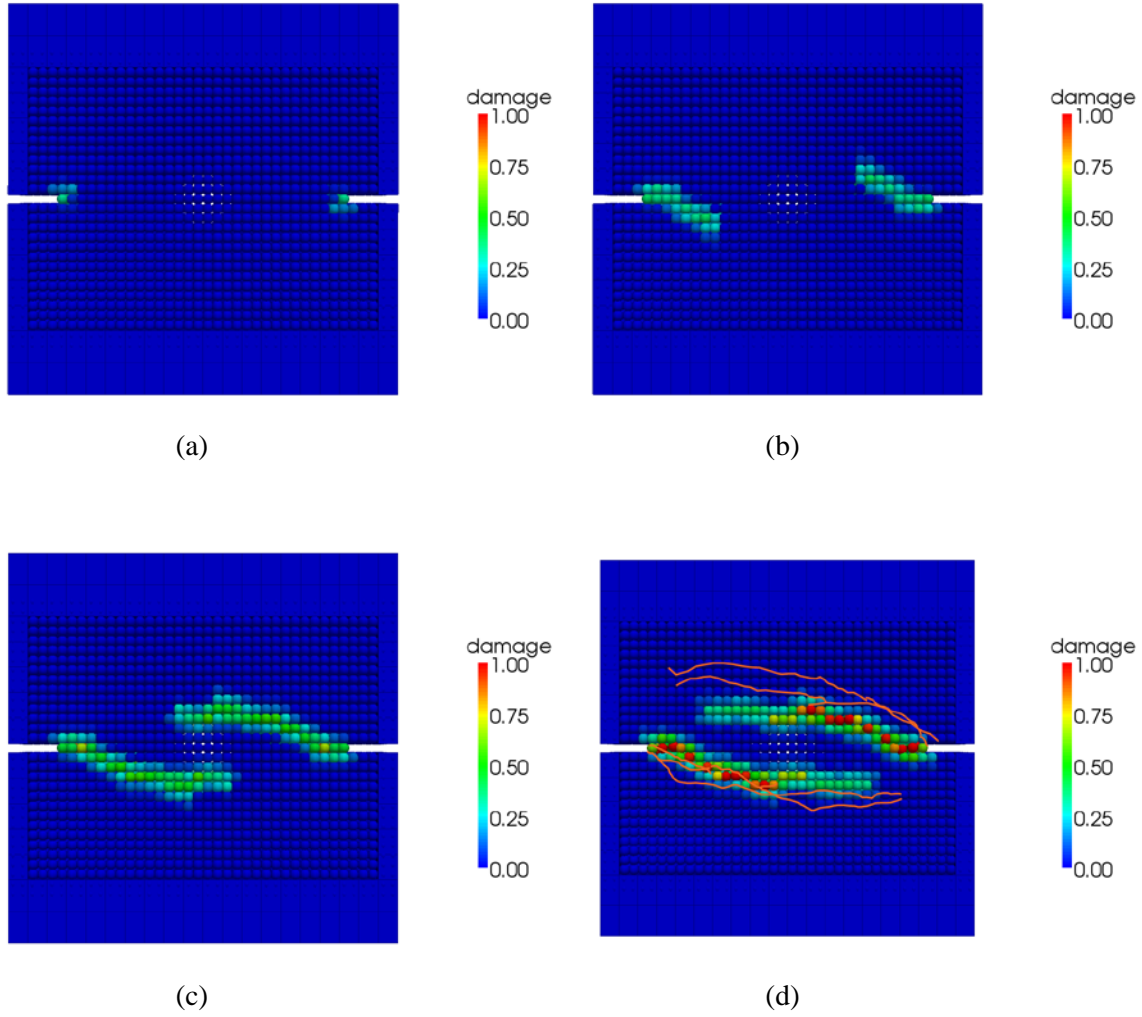
Figure 18: Numerical prediction of crack paths using the CT-coupling scheme. Boundary displacement: (a) $u_n = 0.0220$ mm; (b) $u_n = 0.0225$ mm; (c) $u_n = 0.03$ mm; (d) $u_n = 0.09$ mm. Solid curves are crack paths observed in the experiment [19].

6 Conclusions

A coupling approach of discretized peridynamics with FEM is developed in this research. To bridge conventional FE subregions and peridynamic subregions, an interface element is introduced. The proposed coupling approach is different from other methods in the sense of direct coupling via interface elements. Depending on the size of the horizon, a number of peridynamic nodes are embedded in an interface element. The embedded peridynamic nodes are not involved in the global equation, but essential in the calculation of coupling forces. The coupling forces describe interactions between embedded peridynamic nodes in interface elements and peridynamic nodes in peridynamic subregions. Two types of coupling schemes are introduced. In the VL-coupling scheme, coupling forces on embedded peridynamic nodes are divided to FE nodes of interface elements. On the other hand, coupling forces are divided only to FE nodes on interface segments in the CT-coupling scheme. The inverse isoparametric mapping techniques to determined the natural coordinates of embedded peridynamic nodes in the interface elements and the natural coordinates of projected points on the interface segments are summarized.

Numerical simulations are conducted to compare the computational results using the coupling approach to the classical elasticity solutions. The axial deformation of a one-dimensional bar under quasi-static loading is studied. It is found that the displacements at interfaces of subregions are slightly overestimated, and the displacements in the FE subregions are underestimated using the VL-coupling scheme. On the other hand, the numerical solution using the CT-coupling scheme is almost identical to the quasi-static solution in all subregions and interfaces. For three-dimensional simulations, a bar subjected to quasi-static tension is partitioned into a peridynamic subregion and two FE subregions consisting of eight-node interface elements at both ends of the bar. By measuring displacements at different positions, the CT-coupling scheme is found to be effective in resolving displacements normal to the interface of peridynamic and FE subregions, and the VL-coupling scheme is capable to preserve Poisson effect at the interfaces. Longitudinal strain distributions in the bar and at the interface using the CT-coupling scheme demonstrate good agreement with the quasi-static solution.

The last numerical example is the mixed mode fracture in a concrete specimen subjected to quasi-static loading. The region where failure is expected is modeled using peridynamics, and the remaining region is modeled using conventional FEM to reduce the computational cost. Numerical predictions of crack paths using the VL-coupling scheme and the CT-coupling scheme are studied. Two independent curvilinear crack paths are observed in the results using the CT-couping scheme, and the numerical predictions of crack patterns are close to the experimental observations presented in [19].

References

[1] T. L. Anderson, Fracture mechanics: Fundamentals and applications, CRC, 2005.

[2] G. R. Irwin, Linear fracture mechanics, fracture transition, and fracture control, Engineering Fracture Mechanics 1 (1968) 241-257.

[3] G. R. Irwin, D. E. Wit, A summary of fracture mechanics concepts, Journal of Testing and Evaluation 11 (1983) 56-65.

[4] D. S. Dugdale, Yielding of steel sheets containing slits, Journal of the Mechanics and Physics of Solids 8 (1960) 100-104.

[5] G. I. Barenblatt, The mathematical theory of equilibrium cracks in brittle fracture, Advances in Applied Mechanics 7 (1962) 55-129.

[6] G. Ruiz, A. Pandolfi, M. Ortiz, Three-dimensional cohesive modeling of dynamic mixedmode fracture, International Journal for Numerical Methods in Engineering 52 (2001) 97-120.

[7] J. M. Melenk, I. Babuska, The partition of unity finite element method: basic theory and applications, Computer Methods in Applied Mechanics and Engineering 139 (1996) 289-314.

[8] T. Belytschko, T. Black, Elastic crack growth in finite elements with minimal remeshing, International Journal for Numerical Methods in Engineering 45 (1999) 601-620.

[9] N. Moës, J. Dolbow, T. Belytschko, A finite element method for crack growth without remeshing, International Journal for Numerical Methods in Engineering 46 (1999) 131-150.

[10] J. V. Cox, An extended finite element method with analytical enrichment for cohesive crack

modeling, International Journal for Numerical Methods in Engineering 78 (2009) 48-83.

[11] S. Mariani, U. Perego, Extended finite element method for quasi-brittle fracture, International Journal for Numerical Methods in Engineering 58 (2003) 103-126.

[12] G. Meschke, P. Dumstorff, Energy-based modeling of cohesive and cohesionless cracks via X-FEM, Computer Methods in Applied Mechanics and Engineering 196 (2007) 2338-2357.

[13] S. Li, W. K. Liu, Meshfree and particle methods and their applications, Applied Mechanics Reviews 55 (2002) 1-34.

[14] C. L. Rountree, R. K. Kalia, E. Lidorikis, A. Nakano, L. V. Brutzel, P. Vashishta, Atomistic aspects of crack propagation in brittle materials: Multimillion atom molecular dynamics simulations, Annual Review of Materials Research 32 (2002) 377-400.

[15] H. Gao, Y. Huang, F. F. Abraham, Continuum and atomistic studies of intersonic crack propagation, Journal of the Mechanics and Physics of Solids 49 (2001) 2113-2132.

[16] M. J. Buehler, H. Gao, Dynamical fracture instabilities due to local hyperelasticity at crack tips, Nature 439 (2006) 307-310.

[17] G. R. Liu, Y. T. Gu, Coupling of element free galerkin and hybrid boundary element methods using modified variational formulation, Computational Mechanics 26 (2000) 166-173.

[18] J. W. Hong, K. J. Bathe, Coupling and enrichment schemes for finite element and finite sphere discretizations, Computers & Structures 83 (2005) 1386-1395.

[19] M. B. Nooru-Mohamed, E. Schlangen, J. G. M. van Mier, Experimental and numerical study on the behavior of concrete subjected to biaxial tension and shear, Advanced Cement Based Materials 1 (1993) 22-37.

[20] R. De Borst, Some recent developments in computational modelling of concrete fracture, International Journal of Fracture 86 (1997) 5-36.

[21] M. Di Prisco, L. Ferrara, F. Meftah, J. Pamin, R. De Borst, J. Mazars, J. Reynouard, Mixed mode fracture in plain and reinforced concrete: some results on benchmark tests, International Journal of Fracture 103 (2000) 127-148.

[22] P. Pivonka, J. Ožbolt, R. Lackner, H. A. Mang, Comparative studies of 3D-constitutive models for concrete: application to mixed-mode fracture, International Journal for Numerical Methods in Engineering 60 (2004) 549-570.

[23] T. C. Gasser, G. A. Holzapfel, 3D crack propagation in unreinforced concrete: A two step

algorithm for tracking 3D crack paths, Computer Methods in Applied Mechanics and Engineering 195 (2006) 5198-5219.

[24] J. F. Unger, S. Eckardt, C. Konke, Modelling of cohesive crack growth in concrete structures with the extended finite element method, Computer Methods in Applied Mechanics and Engineering 196 (2007) 4087-4100.

[25] B. Patzák, M. Jirásek, Adaptive resolution of localized damage in quasi-brittle materials, Journal of Engineering Mechanics 130 (2004) 720-732.

[26] J. Réthoré, S. Roux, F. Hild, Mixed-mode crack propagation using a hybrid analytical and extended finite element method, Comptes Rendus M´ecanique 338 (2010) 121-126.

[27] S. A. Silling, Reformulation of elasticity theory for discontinuities and long-range forces, Journal of the Mechanics and Physics of Solids 48 (2000) 175-209.

[28] S. A. Silling, R. B. Lehoucq, Peridynamic theory of solid mechanics, Advances in Applied Mechanics 44 (2010) 73-168.

[29] S. A. Silling, E. Askari, A meshfree method based on the peridynamic model of solid mechanics, Computers & Structures 83 (2005) 1526-1535.

[30] K. Dayal, K. Bhattacharya, Kinetics of phase transformations in the peridynamic formulation of continuum mechanics, Journal of the Mechanics and Physics of Solids 54 (2006) 1811-1842.

[31] W. Gerstle, N. Sau, S. A. Silling, Peridynamic modeling of concrete structures, Nuclear Engineering and Design 237 (2007) 1250-1258.

[32] P. Demmie, S. Silling, An approach to modeling extreme loading of structures using peridynamics, Journal of Mechanics of Materials and Structures 2 (2007) 1921-1945.

[33] B. Kilic, E. Madenci, Structural stability and failure analysis using peridynamic theory, International Journal of Non-Linear Mechanics 44 (2009) 845-854.

[34] Y. D. Ha, F. Bobaru, Studies of dynamic crack propagation and crack branching with peridynamics, International Journal of Fracture 162 (2010) 229-244.

[35] Y. D. Ha, F. Bobaru, Characteristics of dynamic brittle fracture captured with peridynamics, Engineering Fracture Mechanics 78 (2011) 1156-1168.

[36] B. Kilic, E. Madenci, Prediction of crack paths in a quenched glass plate by using peridynamic theory, International Journal of Fracture 156 (2009) 165-177.

[37] A. Agwai, I. Guven, E. Madenci, Predicting crack initiation and propagation using xfem,

czm and peridynamics: A comparative study, in: Electronic Components and Technology Conference (ECTC), 2010 Proceedings 60th, pp. 1178-1185.

[38] S. A. Silling, O. Weckner, E. Askari, F. Bobaru, Crack nucleation in a peridynamic solid, International Journal of Fracture 162 (2010) 219-227.

[39] E. Askari, J. Xu, S. A. Silling, Peridynamic analysis of damage and failure in composites, in: 44th AIAA Aerospace Sciences Meeting and Exhibit, AIAA2006-88, pp. 1-12.

[40] J. Xu, A. Askari, O. Weckner, S. A. Silling, Peridynamic analysis of impact damage in composite laminates, Journal of Aerospace Engineering 21 (2008) 187-194.

[41] B. Kilic, A. Agwai, E. Madenci, Peridynamic theory for progressive damage prediction in center-cracked composite laminates, Composite Structures 90 (2009) 141-151.

[42] W. Hu, Y. D. Ha, F. Bobaru, Modeling dynamic fracture and damage in a fiberreinforced composite lamina with peridynamics, International Journal for Multiscale Computational Engineering 9 (2011) 707-726.

[43] W. Hu, Y. D. Ha, F. Bobaru, Peridynamic model for dynamic fracture in unidirectional fiber-reinforced composites, Computer Methods in Applied Mechanics and Engineering 217 (2012) 247-261.

[44] S. A. Silling, M. Epton, O. Weckner, J. Xu, E. Askari, Peridynamic states and constitutive modeling, Journal of Elasticity 88 (2007) 151-184.

[45] S. A. Silling, R. B. Lehoucq, Convergence of peridynamics to classical elasticity theory, Journal of Elasticity 93 (2008) 13-37.

[46] T. L. Warren, S. A. Silling, A. Askari, O. Weckner, M. A. Epton, J. Xu, A non-ordinary state-based peridynamic method to model solid material deformation and fracture, International Journal of Solids and Structures 46 (2009) 1186-1195.

[47] D. J. Littlewood, Simulation of dynamic fracture using peridynamics, finite element modeling, and contact, in: Proceedings of the ASME 2010 International Mechanical Engineering Congress and Exposition (IMECE), IMECE2010-40621, pp. 209-217.

[48] J. T. Foster, S. A. Silling, W. W. Chen, Viscoplasticity using peridynamics, International Journal for Numerical Methods in Engineering 81 (2009) 1242-1258.

[49] J. T. Foster, S. A. Silling, W. W. Chen, An energy based failure criterion for use with peridynamic states, International Journal for Multiscale Computational Engineering 9 (2011) 675-687.

[50] R. W. Macek, S. A. Silling, Peridynamics via finite element analysis, Finite Elements in Analysis and Design 43 (2007) 1169-1178.

[51] P. Lall, S. Shantaram, D. Panchagade, Peridynamic-models using finite elements for shock and vibration reliability of leadfree electronics, in: Thermal and Thermomechanical Phenomena in Electronic Systems (ITherm), 2010 12th IEEE Intersociety Conference, pp. 1-12.

[52] B. Kilic, E. Madenci, Coupling of peridynamic theory and the finite element method, Journal of Mechanics of Materials and Structures 5 (2010) 707-733.

[53] A. Agwai, I. Guven, E. Madenci, Damage prediction for electronic package drop test using finite element method and peridynamic theory, in: Electronic Components and Technology Conference (ECTC), 2009 Proceedings 59th, pp. 565-569.

[54] E. Oterkus, Peridynamic theory for modeling three-dimensional damage growth in metallic and composite structures, Ph.D. thesis, The University of Arizona., 2010.

[55] G. Lubineau, Y. Azdoud, F. Han, C. Rey, A. Askari, A morphing strategy to couple non-local to local continuum mechanics, Journal of the Mechanics and Physics of Solids 60 (2012) 1088-1102.

[56] W. Liu, J. W. Hong, (in press) Discretized peridynamics for linear elastic solids, Computational Mechanics (2012).

[57] W. Liu, J. W. Hong, Discretized peridynamics for brittle and ductile solids, International Journal for Numerical Methods in Engineering 89 (2012) 1028-1046.

[58] M. L. Parks, S. J. Plimpton, R. B. Lehoucq, S. A. Silling, Peridynamics with LAMMPS: A user guide, Technical Report, Technical Report SAND 2008-1035, Sandia National Laboratories, 2008.

[59] G. T. Mase, R. E. Smelser, G. E. Mase, Continuum mechanics for engineers, CRC, 1999.

[60] K. J. Bathe, Finite element procedures, Prentice Hall, 2006.

[61] W. Liu, J. W. Hong, Three-dimensional lamb wave propagation excited by a phased piezoelectric array, Smart Materials and Structures 19 (2010) 085002.

[62] V. Murti, S. Valliappan, Numerical inverse isoparametric mapping in remeshing and nodal quantity contouring, Computers & Structures 22 (1986) 1011-1021.

[63] V. Murti, Y. Wang, S. Valliappan, Numerical inverse isoparametric mapping in 3D FEM, Computers & Structures 29 (1988) 611-622.

[64] C. Chinnaswamy, B. Amadei, T. H. Illangasekare, A new method for finite element transitional mesh generation, International Journal For Numerical Methods in Engineering 31 (1991) 1253-1270.

[65] J. O. Hallquist, LS-DYNA theory manual, Livermore Software Technology Corporation, Livermore, California, 2006.

[66] P. Wriggers, Computational contact mechanics, Springer, 2006.

[67] H. Moslemi, A. R. Khoei, 3D adaptive finite element modeling of non-planar curved crack growth using the weighted superconvergent patch recovery method, Engineering Fracture Mechanics 76 (2009) 1703-1728.

[68] W. Liu and J. W. Hong, A coupling approach of discretized peridynamics with finite element method, Computer Methods in Applied Mechanics and Engineering 245-256 (2012) 163-175.